Contents list available at CBIORE journal website

International Journal of Renewable Energy Development

Journal homepage: https://ijred.cbiore.id

Research Article

Valorization of olive pruning biomass into high-efficiency activated carbon: CCD optimization and material characterization

Ismaeel Ahmed Nagim, Thouraya Bohli*, Abdemottaleb Ouederni

Research Laboratory: Process Engineering and Industrial Systems, (LR11ES54), National School of Engineers of Gabes, University of Gabes, 6026, Gabes, Tunisia

Abstract. This study focuses on the valorization of olive pruning stems (OPS) biomaterial into a high-efficiency adsorbent. The selected preparation method involved chemical activation using phosphoric acid (H_3PO_4) at a concentration of 50%. The effects of four process parameters: impregnation ratio, impregnation time, carbonization temperature and carbonization time, were studied using Central Composite Design (CCD) to optimize the iodine index, methylene blue index and phenol number of the produced AC. These indexes reflect the development of the AC porosity and its adsorption performances. Obtained results indicate that optimal activated carbon can be prepared under the following conditions: an impregnation ratio of 5.5 g/g, an impregnation time of 7 h, a carbonization temperature of 400°C, and a carbonization time of 1.5 h. Obtained activated carbon in these optimum conditions showed an iodine value of 947 mg/g, methylene blue index exceeding 267 mg/g and phenol number of approximately 35.637 mg/g. Based on the N_2 adsorption–desorption isotherm measurements, the optimized sample exhibited a BET surface area of 1604.8 m^2/g, a total pore volume of 1.124 cm^3/g, and an average pore size diameter of 20.8 nm. These results highlight the suitability of olive pruning rods as a high-quality precursor for producing effective activated carbon, which can be used for wastewater treatment and other applications.

Keywords: Olive pruning stems, Chemical activation, Valorization, Activated carbon, Central Composite Design (CCD), adsorption, iodine index, MB index, phenol index

Received:19th July 2025; Revised: 25th Oct 2025; Accepted: 26th Nov 2025; Available online: 11th Dec 2025

1. Introduction

Activated carbon is an organic porous material widely used in various fields thanks to its exceptional adsorbent properties. It plays a key role in several applications such as water treatment, air pollution control, medicine, and even in the food industry (Maceiras *et al.,* 2017; Gupta and Verma, 2019). Its ability to adsorb a wide range of organic and inorganic compounds from both liquid and gaseous phase makes it indispensable for the removal of pollutants even in trace amounts (Bohli *et al.,* 2025).

An activated carbon adsorbent can be selected based on several critical factors, especially its adsorption capacity, the simplicity of its production processes: determining factor of the cost, and its regenerability. This adsorption performances are mainly attributed to the textural, chemical, and physical properties, including the high specific surface area, well-developed porosity, and the presence of various functional groups on its surface enhancing the adsorption and promoting the eventual desired selectivity. In general, activated carbon with a higher surface area allows for greater adsorption capacity (Kang *et al.,* 2024), while a well-developed pore structure provides efficient pathways for the interaction between adsorbates and the carbon surface (Hassan *et al.,* 2015). Moreover, the presence of oxygenated functional groups such as hydroxyl, carbonyl, and carboxyl groups on the surface of activated carbon enhances its interaction with polar molecules, further improving its adsorptive performances (Bohli *et al.,* 2017; Bhattacharya *et al.,* 2019).

Furthermore, desorption can determine the sustainability and cost-effectiveness of activated carbon as a reused adsorbent after adsorption. Regeneration of an activated carbon can be done via thermal or chemical regeneration process, making it a more economical and environmentally friendly solution (Liu *et al,* 2024; Sun *et al,* 2024). The performance of this step is related to the type of pollutants adsorbed, the regeneration method employed, and the properties of the activated carbon itself (Araujo *et al.,* 2018).

The nature of the raw material used as precursor for activated carbon production affects its final characteristics. The preparation of activated carbon generally involves the use of carbon-rich raw materials, mainly industrial by-products, biomass waste, and lignocellulose agricultural residues such as wood sawdust (Jaria *et al.,* 2019; Devi *et al.,* 2023) , olive stones (Bohli *et al,* 2015), peach stones (Al-Qahtani and Al-Zahrani, 2021), date (Rahman *et al.,* 2025), potato peels (Liu *et al.,* 2023), grenade shells (Saadi et al, 2016), banana peels (Hendronursito *et al,* 2025), orange peels (Kamińska, 2021) etc. However, the use of bio-based raw materials for AC preparation is gaining popularity due to their abundance, low cost, and reduced environmental impact (Yakout and Sharaf El-Deen, 2012). Theses wastes can be transformed into high value-added materials contributing to a circular economy reducing

* Corresponding author
Email: thouraya.bohli@enig.rnu.tn (T.Bohli)

https://doi.org/10.61435/ijred.2026.61589
ISSN: 2252-4940/© 2026.The Author(s). Published by CBIORE

dependence on non-renewable resources (Yaashikaa *et al.,* 2020; Ahmed *et al.,* 2020).

Additionally, the effectiveness of the preparation process, which can include physical or chemical activation methods, plays a significant role in determining the textural properties and functional groups on the carbon internal surface (Tan *et al.,* 2016). Each of these pathways' preparation processes has advantages and disadvantages in terms of cost, complexity, and quality of the final product (Guo *et al.,* 2017). Because of its several advantages, chemical activation was preferred over physical activation. This method requires lower temperature, shorter activation time, and less energy (Alslaibi *et al.,* 2013). Physical activation requires a more complex, two-step process, while chemical activation combines both carbonization and activation into a single step witch also yields activated carbon with a larger specific surface area (Bedia *et al.,* 2020), higher porosity at approximately 3.7 times more than the yield obtainable by physical activation (Balogoun *et al.,* 2015). In addition, often the chemical agents used can be recycled, thus reducing environmental effects. Several parameters influence the preparation of activated carbon via chemical way, including the nature and concentration of the impregnating agent (acid or base), the ratio of the impregnating agent to the precursor material, the duration of the impregnation process, the temperature and time of carbonization, and the flow rate of the inert gas employed during activation (Debbache, 2024)

The choice of the impregnating agent significantly impacts the pore shapes, the pore sizes, and the surface chemistry of the resulting activated carbon. Among acid agents, phosphoric acid (H_3PO_4) sulfuric acid (H_2SO_4) and nitric acid (HNO_3) are widely used in the preparation of activated carbon due to their ability to develop microporous structures while introducing oxygen-containing functional groups on the carbon surface. These properties further enhance its adsorption capacity for polar compounds making it suitable for applications in water treatment and catalysis (González-Serrano *et al.,* 2021; Chen *et al.,* 2022 Ahmed *et al*., 2022).

Phosphoric acid was preferred by some researchers as activating agent due to its very special capabilities for enhancing the properties of activated carbon. It does well in modifying the surface functional groups and pore structure, giving better texture with remarkable ion-exchange capacity. Besides, in both acidic and basic media and at elevated temperatures, it is chemically stable (Balogoun *et al*., 2015). It is an excellent dehydrating agent, hence retards the decomposition process and keeps the volatilization of compounds at a low level leading to high yield of a compact carbon matrix. Its efficiency as an active agent has been widely documented, especially in active carbon outputs from various agricultural by-products, wood, and other carbons, both natural and synthetic (Abdelnaeim *et al.,* 2016). Phosphoric acid makes possible the depolymerization of the macromolecules in biomass, cellulose, hemicellulose, and lignin and crosslink formation by dehydrating and condensing reactions (Abdelnaeim *et al.,* 2016). It also incorporates micropores and mesopores which greatly improve the efficiency of the active carbon in adsorbing micro-organic and inorganic pollutants. Better performance is ascribed to greater porosity, surface area, and pore volume due to the activation process (Ahmed and Theydan, 2012 ; Balogoun *et al.,* 2015).

In contrast, basic agents such as potassium hydroxide (KOH) and sodium hydroxide (NaOH) are known to produce microporous and nanomicropores structures, which are particularly effective for gas separation and energy storage due to their high surface area and narrow pore size distribution (Zhang *et al.,* 2021; Wang *et al.,* 2023). Zinc chloride ($ZnCl_2$) is another commonly used activating agent that promotes the development of both micro- and mesopores, making it ideal for applications such as supercapacitors and pollutant removal (Zhao *et al.,* 2017; Li *et al.,* 2020).

A high concentration of the oxidising agent, whether acidic or basic, generally enhances the development of pore structures but may also lead to excessive etching of the carbon matrix if not carefully controlled (Liu *et al.,* 2015). Moreover, a higher impregnation rate can improve the accessibility of the chemical agent to the precursor, facilitating better pore development. However, prolonged impregnation times may lead to over-saturation, which can negatively affect the structural integrity of the final product (Wang *et al.,* 2023). Furthermore, carbonization temperature and time determine the degree of carbonization and the stability of the activated carbon. Higher temperatures generally promote the formation of a more stable carbon structure, but excessive temperatures can cause pore collapse or excessive burn-off, reducing the surface area (González-García, 2023). The duration of carbonization must also be optimized to ensure complete reaction of the precursor material without degrading the desired porous structure.

The flow rate of the inert gas influences the removal of volatile compounds and the prevention of unwanted oxidation reactions. A controlled flow rate ensures uniform heat distribution and prevents the formation of undesirable by-products, thereby enhancing the quality of the activated carbon (Bansal and Goyal, 2005). Optimizing these parameters is imperative to obtain activated carbon with optimal adsorbent properties. The use of an experimental design, such as a centered composite design, allows this optimization to be systematized by minimizing the number of experimental tests while maximizing the quality of the information obtained (Box and Wilson, 1951). Recent studies have shown that the application of advanced statistical methods, such as response surface methodology (RSM), can significantly improve the efficiency of the production process (Zhang *et al.,* 2021). Among the available RSM-based experimental designs, the Central Composite Design (CCD) is widely regarded as one of the most powerful and flexible tools for multivariate optimization. CCD enables comprehensive evaluation of linear, interaction, and quadratic effects with a reduced number of experimental runs compared to traditional full factorial approaches, thereby minimizing cost and time without compromising model accuracy. In recent years (2019–2024), CCD has become the preferred method for optimizing activated carbon synthesis and adsorption processes due to its high predictive reliability ($R^2 > 0.95$), robustness in modeling nonlinear system behavior, and ability to identify precise optimum conditions (Bayuo *et al.,* 2020; Chen *et al.,* 2024). This design provides an efficient balance between statistical rigor and experimental feasibility, which is critical in studies involving multiple process variables (Khalid *et al.,* 2024). Therefore, CCD was selected in this work as the most suitable and statistically valid framework to determine the optimal preparation conditions for activated carbon, ensuring both experimental efficiency and predictive accuracy.

Tunisia stands out as one of the Mediterranean's leading olive producers, home to approximately 80 million olive trees. Olive tree pruning is a key seasonal activity in Tunisia, that generates a substantial number of branches in various sizes. Large branches are generally used as firewood by farmers or for the production of charcoal, while smaller branches are often left unused. Recent work has shown that agricultural residues, such as those from pruning olive trees, can be efficiently used as

precursor to activated carbon, which provides an environmentally friendly alternative to these types of low-cost local materials (Ponce et al., 2022).

This work explores the valorization of olive pruning biomass resulting from pruning of olive trees as raw material to produce activated carbon, evaluating at laboratory scale the optimal processing conditions to obtain a product with exceptional characteristics. This study aims to optimize the preparation operating parameters of olive pruning stems activated carbon, such as impregnation ratio and time, carbonization temperature, and activation time using RSM based on central composite design (CCD), in order to maximize the specific surface area and developed microporosity of the produced activated carbon and to achieve important adsorption capacity in terms of methylene blue, phenol and iodine indexes.

2. Materials and method

2.1 Materials

Olive pruning residues used in this study were collected from agricultural fields located in the Gabès region of southern Tunisia. This area is characterized by extensive olive cultivation, which generates large quantities of lignocellulosic by-products. These residues represent a readily available and renewable biomass resource with strong potential for conversion and valorization in various environmental and industrial applications. All chemical reagents used were of analytical grade, with high purity levels ranging from 95.5% to 99%. Synthetic solutions were prepared using distilled water.

2.2 Activated carbon fabrication and characterization

2.2.1 Synthesis protocol

The synthesis procedure of activated carbon from olive pruning biomass is begins with biomass pretreatment to enhance its reactivity, then followed by chemical activation using phosphoric acid as the activating agent, which promotes pore development. Finally, the material is subjected to carbonization under controlled conditions to transform the precursor into a highly porous adsorbent with tailored surface characteristics.

First, the collected olive pruning rod was cleaned with distilled water to remove contaminants and subsequently sun-dried to remove moisture. The raw materials were divided into small pieces, rushed, then sieved to obtain a uniform size and stored in ready-to-use glass containers, preparing them for the impregnation process. The impregnation process involves combining a specified quantity of olive pruning rod with a 50% (by weight) phosphoric acid solution in a reaction flask. The mixture was then heated under total reflux at a carefully maintained temperature of 110°C ± 3°C for selected duration Then the impregnated materials were separated from the solution by filtration and dried without rinsing. The dried impregnated precursors were placed in a stainless-steel tubular reactor, 25 cm long and 6 cm in diameter. The reactor is then placed in a horizontal electric furnace with an adjustable temperature and controlled heating. Before the heating process begins, a nitrogen purge is carried out for few minutes to remove any amount of residual oxygen. During the heating process, non–condensable gases and tars are recovered in a trap. Finally, the activated materials were recovered after cooling the latter by gaseous nitrogen stream. At last, obtained activated carbon was washed with hot distilled water to remove phosphoric acid residues and water-soluble suspensions, then dried in an oven at a temperature of 60°C for 24 h to be ready for further tests.

2.2.2. Characterization of Textural and physic-chemical properties

Both the precursor (OPS) and the resulting activated carbon (OPS-AC) underwent comprehensive analysis to evaluate their structural, morphological, and chemical properties. Thermogravimetric analysis (TGA) of the raw material was performed using a simultaneous TGA-DTA instrument (Setaram Instrumentation) under a nitrogen atmosphere with a heating rate of 10°C/min, reaching a maximum temperature of 1000°C. Thermogravimetric analysis (TGA) was applied to study the thermal behavior of the biomass by monitoring changes in mass as a function of temperature and heating rate under controlled conditions. The thermal decomposition of biomass generally occurs in three successive stages: an initial moisture evaporation phase, followed by the devolatilization or active pyrolysis phase, and finally the formation of a carbonaceous residue or char. Some researchers have noted that the active pyrolysis region may consist of two distinct processes, the evolution of volatile compounds and the subsequent oxidation of these volatiles near the particle surface. Overall, TGA provides a precise and efficient approach for evaluating the thermal stability and decomposition characteristics of biomass materials (El-Sayed *et al*., 2024).

Fourier Transform Infrared (FTIR) Spectroscopy was used to qualitatively characterize the functional groups on the surface of olive wood and the resulting activated carbon. FTIR spectra were recorded between 500 and 4000 cm^{-1} using a Perkin Elmer spectrometer. X-ray Diffraction (XRD) analysis was performed using the X'Pert Pro model from Malvern, England. The XRD pattern reveals the level of structural order or disorder in the activated carbon prepared under optimal conditions. The X-ray generator was operating at 40 mA and 45 kV with slow scan rate of 2 per min, and the samples were placed on nickel coated steel holder. Crystallinity of fibers was calculated using the Segal method with Equation (1) as below:

$$\text{Crystallinity Index (\%)} = ((I_{max} - I_{am}) / I_{max}) * 100 \quad (1)$$

Where I_{max} is the intensity height of the highest peak present in the XRD, and Iam is the intensity of the valley between the two crystalline peaks (Trache et al., 2016).

The morphology and porosity of the activated carbon prepared under optimal conditions were analyzed using scanning electron microscopy (SEM) with energy dispersive X-ray (EDX) capabilities. The analysis was conducted with the VP Sigma model from ZEISS, Germany.

2.2.3. Adsorption tests

- *Iodine Index*

The iodine number of the prepared activated carbon was measured by titration based on the standard method ASTM D 4607-94 (ASTM. 2006). The activated carbon sample was treated with 5 wt.% HCl (10.0 mL), boiled for 30 s, and cooled. A 0.1 N iodine solution (100.0 mL) was added, stirred for 30 s, and filtered. The filtrate (50.0 mL) was titrated with 0.1 N $Na_2S_2O_3$ (starch indicator). Adsorbed iodine (X/M, mg/g) was plotted against residual iodine concentration (C, N) on a log-log scale. Tests were repeated with adjusted sample masses if C fell outside 0.008–0.04 N. The iodine number (mg/g) was derived from the regression-fitted X/M value at C = 0.02 N. The X/M and C values are calculated by the equations 2 and 3 respectively using the following expression:

$$\frac{X}{M} = \frac{(N_1*126.93*V_1) - (V_1 + V_{HCl})/V_F)* N_{Na2S2O3}*126.93)*V_{Na2S2O3}}{m_{CA}} \quad (2)$$

$$C = N_{Na2S2O3} * V_{Na2S2O3} \quad (3)$$

where: N_1 is the iodine solution normality; V_1 is the added volume of iodine solution; V_{HCl} is the added volume of 5wt. % HCl; V_F is the filtrate volume used in titration; $N_{Na2S2O3}$ is the sodium thiosulfate solution normality; $V_{Na2S2O3}$ is the consumed volume of sodium thiosulfate solution and m_{CA} is the weight of activated carbon sample.

- *Methylene Blue Index*

The methylene blue index was determined via the methylene blue adsorption method (Raposo et al, 2008). A defined quantity of activated carbon was mixed with a methylene blue solution at a specified concentration, allowing adsorption to reach equilibrium. The residual concentration of methylene blue in the solution was measured using UV spectrophotometry at wavelength of 760 nm. The adsorption capacity was subsequently calculated to obtain the methylene blue index.

- *Phenol index*

The phenol index was determined using a standard method (AWWA B600-90 index). In this procedure, 0.3 g of dry activated carbon was mixed with 100 ml of a 0.1 g/L phenol solution and stirred at 25°C for 24 hours. The remaining phenol concentration was then measured by UV spectrophotometry at 269 nm, following a calibration curve. The calculation formula of phenol is the same as for the methylene blue index (Eq.4):

$$q_t = \frac{(C_0 - C_f)}{m_{CA}} V_{sol} \quad (4)$$

where qe is adsorbed quantity (mg/g); C0 and Cf are the initial and residual concentrations (mg/L); mCA is the activated carbon masse (g) and Vsol is the solution volume.

2.4. Experimental design and data analysis

The optimisation of activation and carbonization experimental parameters was studied using response surface methodology (RSM) and multi-criteria optimization with central composite design (CCD). This method helps to evaluate the individual and interaction effects of studied factors and then estimate their optimal values. Commercial software (Design-Expert, version 13) was employed for the analysis, chosen for its ability to efficiently handle second-order polynomial models and interaction effects, streamlining the response surface methodology (RSM) process.

Four variables were considered in this study; the impregnation ratio (X_1), impregnation time (X_2), carbonization temperature (X_3) and carbonization time (X_4). Table 1 summarizes the experimental examined range of each variable determined based on preliminary experimental studies. Three responses were considered to evaluate the quality of the prepared activated carbon; the iodine number (Y_1), methylene blue index (Y_2), and phenol number (Y_3) were analysed as responses.

The optimal predictive model was determined through quadratic regression analysis, supported by ANOVA (Analysis of Variance) and F-statistics. The relationship between input parameters and response variables was mathematically represented using a second-order polynomial regression equation (5) (Lix *et al.,* 1996; Arokiadass *et al.,* 2012; Chelladurai *et al.,* 2021):

$$\hat{Y} = \beta_0 + \sum_{i=1}^{k} \beta_i x_i + \sum_{i=1}^{k} \beta_{ii} x_i^2 + \sum_{i<j}^{k} \beta_{ij} x_i x_j \quad (5)$$

where Y is the response; k the number of variables; xi and xj the coded values of the factors; and β_0, β_i, β_{ii}, and β_{ij} are the constant coefficient, the linear coefficient, the quadratic coefficient, and the interaction coefficient, respectively.

The center points were repeated three times to estimate experimental error variance and assess data reproducibility. To minimize the impact of systematic errors, experiments were conducted in random order. Model validation involved analysis of variance (ANOVA), and further evaluation was performed using the correlation coefficient (R^2) and the adjusted determination coefficient (R^2_A), both of which indicate the proportion of total observed variability explained by the model. An analysis of variances (ANOVA) was performed to confirm the most appropriate models applied at the 95% confidence level (Liu *et al.,* 2021). The effect of a factor is considered to be the variation in the response caused by an adjustment in the level of the factor.

.

3. Results and discussion

3.1 Characterization of the raw material

3.1.1 Thermogravimetric analysis

The TGA/DTG curves for olive pruning stems under nitrogen flow are shown in Figure 1. The initial endothermic event, below 200°C, corresponds to the drying phase, during which moisture is released from the material (Lütke *et al.*, 2019). This phase results in a slight weight loss, reflecting the removal of residual water. The second phase of mass loss occurs between 200°C and 380°C, marked by a significant slope in the TG curve. This stage is characterized by the liberation of volatile hydrocarbons from the thermal degradation of hemicellulose, cellulose, and parts of lignin. Hemicellulose begins to decompose at lower temperatures, followed by cellulose degradation, which is observed as a pronounced change in the curve slope, indicative of a shift in chemical kinetics. In the third phase, from 380°C to approximately 600°C, weight loss becomes less pronounced. This phase is associated with the gradual decomposition of lignin; a more thermally

Table 1
Experimental variables with defined low and high levels

Code	Variables	Unit	Low level	High level
X_1	Impregnation rate (phosphoric acid solution weight/ OPS weight)	g/g	4	6
X_2	Impregnation time	h	4	8
X_3	Carbonization temperature	°C	350	550
X_4	Carbonization time	h	1	3

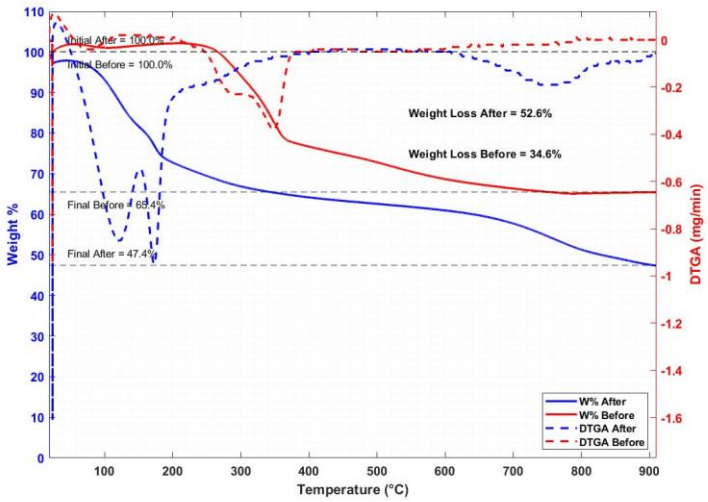

Fig. 1 Thermal analysis (TG/DTG) of OPS before and after impregnation.

stable compound compared to hemicellulose and cellulose (El-Sayed *et al.,* 2024). The minor slope beyond 600°C suggests the formation of char, as lignin exhibits a greater tendency to resist complete decomposition and instead contributes to residual carbonaceous material. The evolution of the heat flow generated during the bio material pyrolysis shows that the different steps proposed are exothermic.

The effect of impregnation reveals a thermal profile comparable to that of untreated samples (OPS) (Figure 1). The thermogravimetric study of impregnated olive pruning stems pyrolyzed under nitrogen at 5°C/min reveals three distinct degradation stages. The initial phase (50-75°C) corresponds to moisture evaporation and gas desorption, consistent with observations in similar lignocellulosic materials (Paz et al., 2023; El-Sayed *et al.,* 2024). As compared to no impregnated raw material, the second step held bat low temperature between 75-200°C with a significant 8% mass loss, primarily attributed to macromolecular decomposition and depolymerization - a critical process for pore structure development in carbon-based materials. The final stage (>200°C) shows gradual mass loss, where simultaneous volatile release and aromatic condensation promote microporous network formation, as previously reported in agricultural waste conversion studies (Jeguirim et al., 2020). This dual mechanism enhances specific surface area and adsorption capacity in the resulting activated carbon.

3.1.2 Spectrophotometric FTIR analysis

The FTIR spectrum of OPS is shown in Figure 2. This spectrum exhibits absorption bands primarily associated with hydroxyl and carbonyl groups. The broad absorption bands around 3417 cm^{-1} and 3777 cm^{-1} are attributed to hydrogen-bonded O–H groups found in cellulose, pectin, and lignin. The bands observed at approximately 2924 cm^{-1} and 2855 cm^{-1} correspond to symmetric and asymmetric C–H stretching in methyl and methylene groups. The band at 1460 cm^{-1}

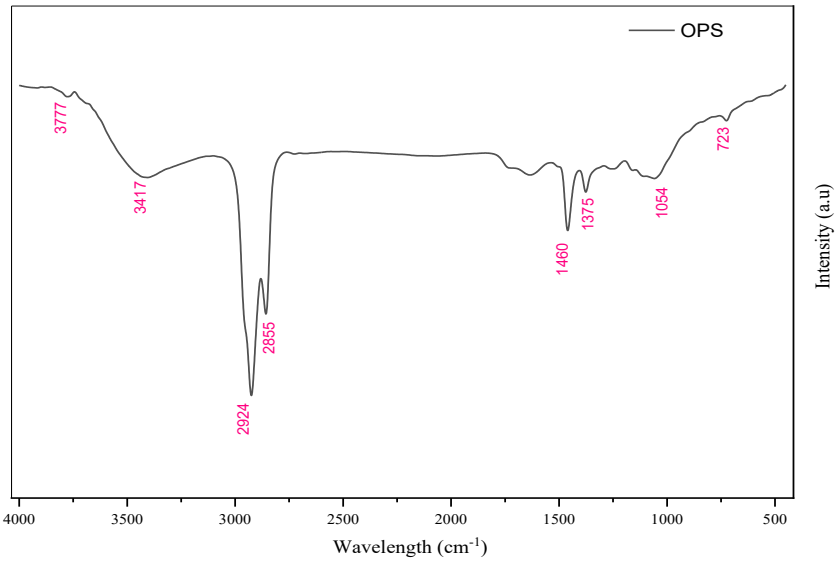

Fig 2: FTIR spectrum of olive pruning stems

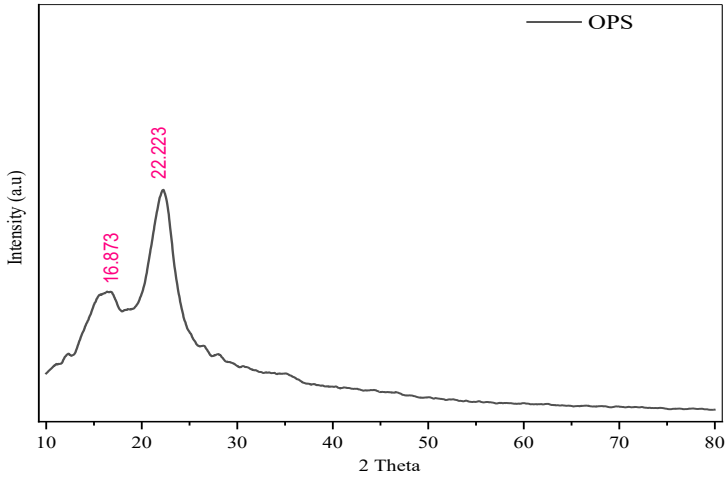

Fig. 3 X-ray diffraction (XRD) pattern of raw OPS

Table 2
XRD parameters for each peak

No.	2 Theta (°)	FWHM	d-spacing (nm)	Relative Intensity (%)	Crystal Size (nm)
1	15.037	1.7042	0.576	21.34	4.9124
2	16.873	1.27201	0.526	26.24	4.6642
3	22.223	2.0763	0.398	100.0	3.7804

corresponds to the aliphatic and aromatic C–H vibration in planar deformation of methyl, methylene, and methoxy groups. The band at 1375 cm^{-1} is associated with the in-plane bending of CH, enolic C–OH, and skeletal C–C–C vibrations. Bands around 1250 cm^{-1} and 1054 cm^{-1} are ascribed to C–O stretching and O–H bending vibrations in carboxylic acids and alcohols, The weak band observed at 723 cm^{-1} is attributed to the out-of-plane C–H bending vibration in aromatic structures.

3.1.3 X-Ray diffraction analysis

The X-ray diffraction (XRD) pattern for raw olive pruning stems (OPS) is shown in Figure 3. The XRD diffractogram displays a prominent peak at 2θ = 16.37° (plan 110) and at 2θ = 22.22° (plan 200) confirming the crystalline structure of cellulose-I. The first one Indicates the lateral packing arrangement of cellulose microfibrils and the second one reflects the tightly packed cellulose chains along the (200)

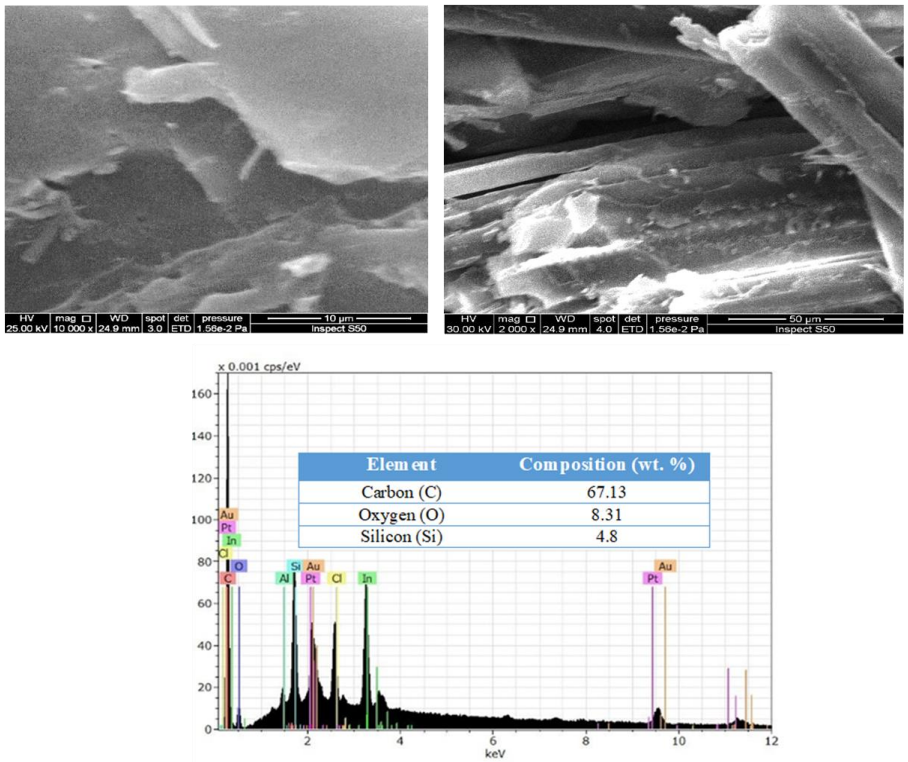

Fig. 4 SEM images and EDX analysis results of raw olive pruning stems.

lattice plane, indicates a high level of a microcrystallinity (Trache et al., 2016). These peaks, along with other key XRD parameters such as FWHM, d-spacing, relative intensity, and crystal size for each observed peak, is summarized in Table 2. These sharp peaks signify a high degree of crystallinity associated with the cellulose content in the sample. The crystallinity index was calculated using Segal's equation, resulting in a value of 56.08%.

This value suggests a partially crystalline nature of OPS, with a predominant amorphous structure and a minor crystalline component. Secondary peaks in the diffractogram correspond to other structural components, such as lignin variants, which contribute to the overall amorphous character. Additionally, OPS exhibits a low ash content of 5.43%, indicating its suitability for activated carbon production and suggesting its potential as a valuable raw material for high-performance applications.

Characterization results show that olive pruning stems (OPS) has structural and compositional properties ideal for advanced applications. Thermal analysis (TG/DTG), along with FTIR and X-ray diffraction (XRD) analysis, indicates that OPS is suitable as a precursor for hard activated carbon, especially for wastewater treatment application, where high carbon content and stability are essential.

3.1.4. Micrography SEM observation

Figure 4 shows the scanning electron micrographs (SEM) of the surface of the olive pruning stems. It presented a well-defined and irregular structure, maintaining their original morphology, indicating the good thermo-mechanical stability of the raw material. The image highlights the presence of voids, cracks, and an irregular surface morphology. These features suggest the natural heterogeneity of olive wood, with observable porosity likely corresponding to cell lumens, vessel walls, and microfibrillar arrangements. The SEM image provides a broader view of the olive pruning stem's microstructure, showcasing elongated, fiber-like formations and interconnected channels. These features are characteristic of the cellular

Table 3
Central composite design matrix, exprimental conditions and observed responses

Experiment no.	X_1	X_2	X_3	X_4	Y_1	Y_2	Y_3
1	4.5	5	400	1.5	667.96	259.704	26.340
2	5.5	5	400	1.5	740.22	252.392	27.519
3	4.5	7	400	1.5	816.77	261.280	30.630
4	5.5	7	400	1.5	738.32	263.212	22.800
5	4.5	5	500	1.5	736.25	246.130	33.146
6	5.5	5	500	1.5	746.78	267.314	28.700
7	4.5	7	500	1.5	937.72	260.136	26.620
8	5.5	7	500	1.5	674.98	247.072	22.068
9	4.5	5	400	2.5	736.25	246.130	33.146
10	5.5	5	400	2.5	725.68	250.032	24.497
11	4.5	7	400	2.5	947.13	267.258	35.637
12	5.5	7	400	2.5	737.92	244.154	15.151
13	4.5	5	500	2.5	636.82	249.638	28.718
14	5.5	5	500	2.5	670.04	252.616	34.266
15	4.5	7	500	2.5	687.46	262.318	30.646
16	5.5	7	500	2.5	736.25	246.130	33.146
17	5	6	450	2	853.16	254.598	31.415
18	5	6	450	2	835.08	264.960	28.856
19	5	6	450	2	655.22	262.522	35.018
20	4	6	450	2	720.42	254.618	24.435
21	6	6	450	2	790.27	267.724	28.722
22	5	4	450	2	764.78	251.946	25.294
23	5	8	450	2	720.25	260.980	28.128
24	5	6	350	2	706.80	254.946	29.065
25	5	6	550	2	708.26	260.901	24.794
26	5	6	450	1	785.07	251.624	28.663
27	5	6	450	3	683.50	266.982	27.485

structure of lignocellulosic materials, including vessel elements and fibrous tissues. The hierarchical arrangement of the fibers is clearly visible, reflecting the anisotropic and porous nature of the olive pruning biomass This description emphasizes the observed features, connects them to the natural structure of lignocellulosic materials. The mains compositions of raw material are carbon (67.13%), oxygen (8.31%), and silicon (4.80%), as given by EDX. The others compositions may be attributed to the contamination by the equipment of the carbonization or the analysis preparations.

3.2. Model results and statistical analysis

3.2.1. Evaluation of the responses

Following the Central Composite Design (CCD) framework, experimental trials were conducted, and the resulting response values are presented in Table 3. The experimental setup included 27 randomized runs, consisting of 16 factorial points (full 2^4 design), 8 axial (star) points, and 3 replicated center points to evaluate experimental error and curvature effects.

Analysis of variance (ANOVA) derived from Response Surface Methodology (RSM) was employed to develop a quadratic polynomial regression model. This model quantitatively assesses the impact of the independent variables on the three target responses: the iodine number (Y_1), methylene blue index (Y_2), and phenol number (Y_3).

The finalized predictive equations, expressed in coded factors, are represented by the following second-order polynomial expressions:

$$\mathbf{Y_1} = 736.25 + 14.20\ X_1 + 17.87\ X_2 - 53.43\ X_3 - 43.93\ X_4 - 21.56\ X_2X_3 - 22.18\ X_2X_4 + 21.71\ X_3X_4 + 5.8\ X_1^2 - 5.32\ X_2^2 + 5.5\ X_3^2 + 5.71\ X_4^2 \quad (6)$$

$$\mathbf{Y_2} = 246.13 - 4.63X_4 + 3.32X_1X_2 + 2X_2X_3 - 1.57X_2X_4 + 1.24X_1^2 + 4.8X_2^2 + 3.17X_3^2 + 2.53X_4^2 \quad (7)$$

$$\mathbf{Y_3} = 33.15 + 0.789X_1 - 1.04\times X_2 + 0.964\times X3 - 1.5\ X_4 + 1.51\ X1X_2 - 2.31\ X_1\ X_3 - 1.55X_2X_4 + 2.21X_3X_4 - 1.61X_1X_2 - \mathbf{1}.97X_2^2 - 1.89X_4^2 \quad (8)$$

The analysis of variance (ANOVA) results (Table 4) demonstrate that the developed quadratic models for iodine number (Y_1), methylene blue index (Y_2), and phenol index (Y_3) were all statistically significant ($p < 0.0001$), with F-values of 97.43, 21.81, and 59.04 respectively. These high F-values and extremely low p-values confirm that the models adequately represent the experimental data and can reliably predict the adsorption behavior of activated carbon that reflect the textual characters specially porosity and specific surface. The nonsignificant lack of fit ($p > 0.05$) for all three responses further validates the model adequacy, indicating no unexplained variation in the experimental design.

- Adsorption capacity for iodine (Y_1)

The iodine adsorption test is widely employed as an indicator of the adsorption capacity of activated carbon for impurities. For wastewater treatment applications, the recommended minimum iodine number generally falls between 636.82 and 947.132 mg/g, with higher values indicating greater adsorption efficiency, essential for effective contaminant removal (Bansal and Goyal, 2005; Louarrat et al., 2019). This number is also a recognized measure of activated carbon's microporosity, as higher values reflect increased microporosity

Table 4
ANOVA and statistical values for activated carbon synthesi

Source	Y1 : Iodine Index					Y2 : MB index					Y3 : Phenol index				
	Sum of Squares	DF	Mean Square	F-value	p-value	Sum of Squares	DF	Mean Square	F-value	p-value	Sum of Squares	DF	Mean Square	F-value	p-value
Model	1.536E+05	14	10974.77	97.43	< 0.0001	1423.85	14	101.70	21.81	< 0.0001	520.29	14	37.16	59.04	< 0.0001
X_1	4842.26	1	4842.26	42.99	< 0.0001	8.37	1	8.37	1.80	0.2051	14.90	1	14.90	23.67	0.0004
X_2	7659.87	1	7659.87	68.00	< 0.0001	7.27	1	7.27	1.56	0.2358	25.75	1	25.75	40.91	< 0.0001
X_3	68525.26	1	68525.26	608.34	< 0.0001	6.19	1	6.19	1.33	0.2716	22.30	1	22.30	35.43	< 0.0001
X_4	46305.91	1	46305.91	411.09	< 0.0001	514.37	1	514.37	110.30	< 0.0001	53.85	1	53.85	85.54	< 0.0001
X_1X_2	73.27	1	73.27	0.6504	0.4357	166.65	1	166.65	35.74	< 0.0001	36.40	1	36.40	57.83	< 0.0001
X_1X_3	66.66	1	66.66	0.5918	0.4566	7.66	1	7.66	1.64	0.2242	85.62	1	85.62	136.02	< 0.0001
X_1X_4	61.30	1	61.30	0.5442	0.4749	9.56	1	9.56	2.05	0.1778	7.656 E-07	1	7.656E-07	1.216 E-06	0.9991
X_2X_3	7436.56	1	7436.56	66.02	< 0.0001	63.76	1	63.76	13.67	0.0030	0.3707	1	0.3707	0.5889	0.4577
X_2X_4	7867.78	1	7867.78	69.85	< 0.0001	39.57	1	39.57	8.48	0.0130	38.42	1	38.42	61.03	< 0.0001
X_3X_4	7543.88	1	7543.88	66.97	< 0.0001	21.81	1	21.81	4.68	0.0515	78.01	1	78.01	123.93	< 0.0001
X_1^2	717.09	1	717.09	6.37	0.0268	32.60	1	32.60	6.99	0.0214	55.27	1	55.27	87.80	< 0.0001
X_2^2	603.45	1	603.45	5.36	0.0392	492.22	1	492.22	105.55	< 0.0001	82.71	1	82.71	131.39	< 0.0001
X_3^2	645.68	1	645.68	5.73	0.0339	214.27	1	214.27	45.95	< 0.0001	0.0524	1	0.052	0.0833	0.7778
X_4^2	695.91	1	695.91	6.18	0.0287	136.90	1	136.90	29.36	0.0002	76.13	1	76.13	120.94	< 0.0001
Residual	1351.72	12	112.64			55.96	12	4.66			7.55	12	0.629		
Lack of Fit	1351.72	10	135.17			55.96	10	5.60			7.55	10	0.755		
Pure Error	0.0000	2	0.0000			0.0000	2	0.0000			0.0000	2	0.000		
Cor Total	1.550 E +05	26				1479.81	26				527.84	26			

and a larger internal surface area. The iodine index values observed in this study ranged from 636.82 to 947.13 mg/g, demonstrating substantial porosity across all prepared samples (Table 2). Correlation coefficients relative to (Eq.5), R^2 = 0.950 and R^2 adjusted = 0.981 (Table 3), between the maximum adsorption capacities calculated by the model and those determined experimentally indicate a satisfactory fit. Analysis of the response Y_1 shows that the impregnation ratio (X_1) and impregnation time (X_2) have a strong impact on the adsorption capacity of iodine. The positive coefficients for these parameters indicate that increasing X_1 and X_2 enhances the adsorption capacity, suggesting their importance in developing effective adsorption characteristics. Specifically, an increase of 14.20 units in Y_1 per unit increase in X_1 and 17.87 units in Y_1 per unit increase in X_2 highlight their beneficial role.

In contrast, carbonization temperature (X_3) and carbonization time (X_4) have negative impacts on Y_1, as evidenced by their negative coefficients (-53.43 and -43.93, respectively). This indicates that higher carbonization temperatures and longer carbonization times reduce the adsorption capacity, potentially due to detrimental effects on the porous structure of the activated carbon. The interaction between parameters further illustrates the complexity of the system. The negative interactions between impregnation time (X_2) and carbonization temperature (X_3), as well as between impregnation time (X_2) and carbonization time (X_4), suggest that simultaneous increases in these parameters can reduce adsorption efficiency. Conversely, the positive interaction between X_3 and X_4 implies that increasing both parameters together might have a compensatory effect, mitigating some of their individual negative impacts. The quadratic terms also provide insights into the optimization of the parameters. The positive values for X_1^2, X_3^2, and X_4^2 indicate that there might be a beneficial range for these parameters, beyond which adsorption capacity improves. On the other hand, the negative coefficient for X_2^2 suggests the existence of an optimal impregnation time, beyond which further increases could negatively affect adsorption.

Figure 5 illustrates the interaction between two independent variables in contour plots. Figure 5-(a) shows the combined effect of impregnation time (X_2) and carbonization temperature (X_3) on the iodine number (Y_1). The highest iodine number, approximately 947 mg/g, was achieved at a carbonization temperature of 400°C and an impregnation time of 7 hours. The figure suggests that both parameters play a significant role in enhancing iodine adsorption, with increasing impregnation time and a suitable carbonization temperature leading to greater pore development and improved adsorption capacity. Figure 5-(b) depicts the correlation between impregnation duration (X_2) and carbonization duration (X_4) about the iodine number (Y_1). Following 7 hours of impregnation and around 2.5 hours of carbonization, the maximum iodine number of 947 mg/g is attained. The graphic demonstrates that extended carbonization durations generally maintain the iodine number, whereas prolonged impregnation durations positively influence it. This suggests that although structural growth requires adequate carbonization, excessive carbonization may lead to declining rewards in terms of iodine adsorption.

Figure 5-(c) shows how the iodine number (Y_1) is affected by the carbonization temperature (X_3) and time (X_4). The figure shows that the iodine number remains rather consistent across the range of carbonization temperatures and durations, with values averaging roughly 700 mg/g. This suggests that, within the given parameter range, changes in the carbonization temperature or duration have no appreciable effect on the iodine number. This could be because at high temperatures or carbonization times, stabilizing effects and pore enlargement cancel out any additional pore formation.

- *Methylene blue index (Y_2)*

One important indicator of activated carbon's suitability for wastewater treatment is the methylene blue index (MBI). The MBI measures the adsorption capacity of activated carbon, particularly for medium- to large-sized molecules, to determine how successfully it removes organic materials from aqueous solutions, such as colors and pollutants. This index is commonly used to assess the surface area and mesoporosity of activated carbon since it shows the material's ability to adsorb larger molecules. In order to compare and assess the adsorptive performance of activated carbons derived from various precursors for specific water purification applications, the MBI is widely utilized. Methylene blue index values for the investigation ranged from 244.15 to 267.724 mg/g (Table 2).
The correlation coefficients of (Eq.8), R^2=0.962 and $R^2_{adjusted}$=0.918 (Table 3), indicate that the model provides a strong fit to the experimental data, capturing over 96% of the variability in adsorption capacity. This high level of fit suggests that the model is reliable for predicting Y_2 within the specified parameter ranges.

Analysis of this response (Y_2) shows that the carbonization time (X_4) has a notable influence on the adsorption capacity of methylene blue, as demonstrated by its negative coefficient. This suggests that extended carbonization time may adversely

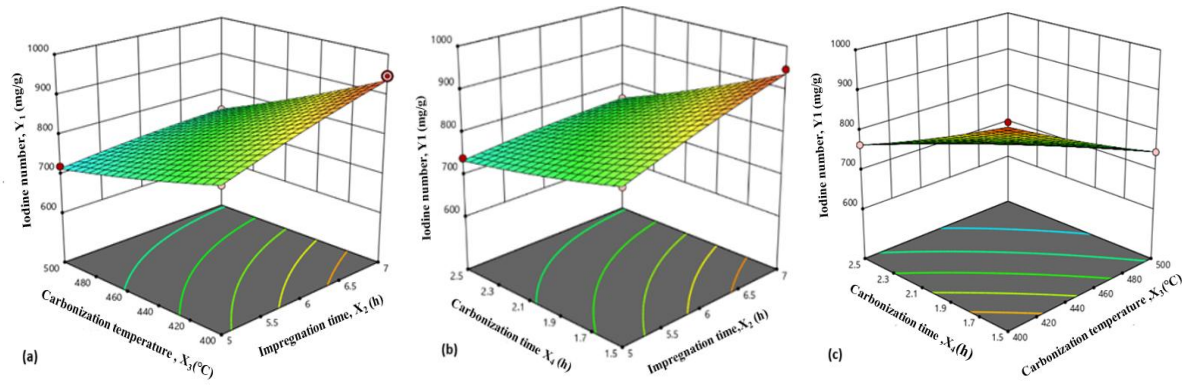

Fig. 5 3D response surface for response iodine number (Y1): impregnation time (X_2) and carbonization temperature (X_3) (a), impregnation time (X_2) and carbonization time (X_4) (b), carbonization temperature (X_3) and carbonization time (X_4) (c).

affect the porous structure necessary for effective adsorption. Additionally, the positive interaction between impregnation rate (X_1) and impregnation time (X_2) suggests a synergistic effect, where simultaneous increases in these parameters enhance the adsorption capacity of the activated carbon. Similarly, the positive interaction between impregnation time (X_2) and carbonization temperature (X_3) further indicates that increased values of these factors together improve adsorption performance, possibly through optimized pore formation. However, the negative interaction between impregnation time (X_2) and carbonization time (X_4) suggests a complex interplay, where simultaneous increases in these factors may reduce adsorption efficiency, likely due to structural alterations at prolonged exposure. The quadratic terms provide additional insights, with the positive values for X_1^2, X_2^2, X_3^2, and X_4^2 indicating an optimal range for each parameter, beyond which the adsorption capacity is maximized. This analysis underscores the importance of balancing the impregnation and carbonization conditions to enhance the adsorptive performance of activated carbon for methylene blue.

Figure 6-(a) shows the combined effect of impregnation rate (X_1) and impregnation time (X_2) on the methylene blue index (MBI). The highest MBI was observed at an impregnation rate of approximately 5.5 g/g and an impregnation time of 7 hours. The figure indicates that MBI increases with a higher impregnation rate and a longer impregnation time. This suggests that these conditions promote the development of an optimal pore structure in the activated carbon, hence facilitating improved adsorption of methylene blue molecules. The material's adsorptive capacity is likely increased by the faster impregnation rate, which facilitates the growth of larger, more accessible pores.

Figure 6-(b) shows how the methylene blue index (Y_2), which measures adsorption capacity, is impacted by the carbonization temperature (X_3) and impregnation duration (X_2). The surface plot indicates that the methylene blue index (MBI) peaks after 7 hours of impregnation and at a carbonization temperature of roughly 400°C. The MBI shows a consistent increase with increasing temperature and small impregnation times, indicating that higher temperatures enhance porosity, which in turn enhances adsorption. The regions with the highest MBI and the optimal conditions for achieving high adsorption capacity are shown by the base contour lines.

Figure 6-(c) illustrates how the carbonization temperature (X_3) and impregnation time (X_2) affect the methylene blue index (Y_2), which gauges adsorption capability. According to the surface plot, the methylene blue index (MBI) peaks at a carbonization temperature of about 400°C and seven hours after impregnation. Higher temperatures improve porosity, which in turn improves adsorption, as evidenced by the MBI's steady rise with rising temperature and brief impregnation periods. The base contour lines indicate the areas with the highest MBI and the ideal circumstances for reaching high adsorption capacity.

In conclusion, the analysis of Figures 6 (a), (b) and (c) show that the interaction between impregnation rate, impregnation time, carbonization temperature, and carbonization time has a significant impact on the methylene blue index (MBI). When the carbonization temperature is about 400°C, the carbonization time is roughly 1.5 hours, the impregnation rate is about 5.5 g/g, and the impregnation time is about 7 hours, the best MBI values are obtained. These particular circumstances contribute to the development of a pore structure that enhances adsorption capacity. On the other hand, an excessively extended carbonization time may harm the pore structure and lower adsorption effectiveness. This finding highlights the importance of carefully adjusting impregnation and carbonization conditions to get the most effective adsorption results from activated carbon.

- *Phenol index (Y_3)*

The phenol index is a crucial metric for determining if activated carbon is suitable for treating wastewater. The phenol index indicates how well activated carbon removes phenols and other related organic contaminants from aqueous solutions by measuring its capacity to adsorb phenolic chemicals. When evaluating the microporous structure of activated carbon, this metric is especially helpful because phenolic chemicals are tiny molecules. In applications where phenolic pollutants are an issue, such industrial effluent treatment and water purification, the phenol number is frequently used to compare the performance of activated carbons made from different precursors.

The phenol index values observed in this study ranged from 15.151 to 35.6375 mg/g (Table 2). The phenol adsorption capacity (Y_3) of activated carbon can be accurately described using a second-order polynomial equation, which includes linear, interaction, and quadratic terms. This model offers a robust framework for analyzing the impact of critical experimental parameters on the adsorption efficiency of activated carbon in wastewater treatment processes.

The high R^2 value (0.986) and adjusted R^2 (0.969), corresponding of Y_3 (Eq.7), demonstrate the model's strong fit to the experimental data, while the predicted R^2 (0.918) confirms its reliability for predicting new outcomes.

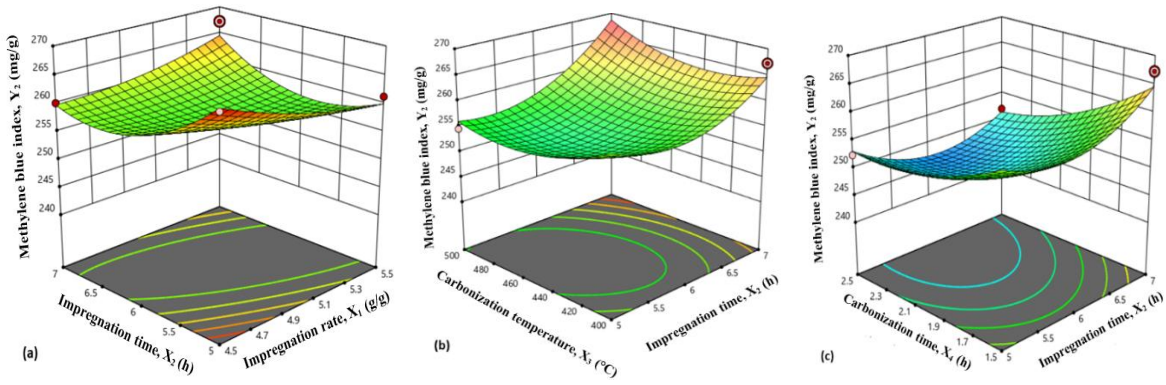

Fig. 6 3D response surface for response methylene blue index (Y2): impregnation rate (X_1) and impregnation time (X_2) (a), impregnation time (X_2) and carbonization temperature (X_3) (b), impregnation time (X_2) and carbonization time(X_4) (c).

Positive linear effects of $X_1$and X_3 indicate their direct contributions to enhancing phenol adsorption, while negative interaction and quadratic terms suggest the importance of optimizing variable combinations to avoid diminishing returns. The analysis of this response (Y_3) shows that, as evidenced by its negative linear coefficient, carbonization time (X_4) significantly affects activated carbon's ability to adsorb phenol. This implies that the microporous structure necessary for effective phenol adsorption may be adversely affected by prolonged carbonization time. A synergistic impact is highlighted by the positive interaction between impregnation rate (X_1) and impregnation time (X_2), whereby concurrent increases in these parameters increase adsorption capacity, most likely as a result of improved precursor activation. Similarly, the fact that carbonization temperature (X_3) and carbonization duration (X_4) have a positive relationship implies that both variables, when controlled in tandem, improve pore formation and adsorption efficiency.

On the other hand, the negative correlation between carbonization temperature and impregnation rate suggests that high values of both parameters at the same time may reduce adsorption effectiveness, possibly as a result of mesopore overdevelopment at the expense of micropores. The quadratic terms highlight the necessity of keeping these parameters within an ideal range by showing diminishing profits at extreme values, especially for X_1^2, X_2^2, and X_4^2. This analysis emphasizes how important it is to strike a balance between carbonization and impregnation parameters in order to optimize activated carbon's adsorption capability for phenol removal. The model is accurate and reliable, providing a useful tool for maximizing phenol removal in wastewater treatment applications by streamlining activated carbon preparation procedures.

Based on the analysis, it can be observed that the phenol adsorption capacity (Y_3) is more efficient when the impregnation rate (X_1) and carbonization temperature (X_3) are high, as both parameters positively influence adsorption. Conversely, minimizing the impregnation time (X_2) and carbonization time (X_4) is advantageous, as their extended durations negatively influence the adsorption capacity. This suggests that optimizing these parameters by balancing high values of X_1 and X_3 with minimal X_2 and X_4 can maximize the phenol index, ensuring more effective adsorption performance of the activated carbon.

Figure 7-(a) illustrates the interaction between impregnation time (X_1) and impregnation rate (X_2) on the phenol index (Y_3). The surface plot shows a peak phenol index around an impregnation rate of approximately 5.5 g/g and an impregnation time of 7 hours. The plot indicates that the phenol index improves with an increase in both variables, up to a certain threshold. This pattern implies that longer impregnation periods and rates improve the material's pore structure, boosting adsorption effectiveness. The contour projection highlights the ideal area for obtaining high adsorption performance by showing the region where the phenol index is maximum.

The combined effects of carbonization temperature (X_3) and impregnation rate (X_1) on the phenol index (Y_3) are shown in Figure 7-(b). At a carbonization temperature of about 400°C and an impregnation rate of roughly 5.5 g/g, the greatest phenol index is recorded. According to the surface plot, the phenol index rises with both factors, reaches an ideal range, and then starts to fall. While higher carbonization temperatures promote the formation of pore structures, too high of a temperature can cause structural deterioration and lower adsorption capability. Similar to this, a suitable impregnation rate guarantees adequate activation, while too high of one might result in structural instability or pore blockage. In order to get optimum performance, the contour projection emphasizes the region of optimal adsorption capacity and the crucial balance between carbonization temperature and impregnation rate.

Using a 3D response plot, Figure 7-(c) illustrates how the carbonization time (X_4) and impregnation time (X_2) interact with the phenol index (Y_3). After about seven hours of impregnation and one and a half hours of carbonization, the phenol index peaks. Longer impregnation times have a beneficial effect on the phenol index, however longer carbonization times reduce adsorption efficiency, as the figure illustrates. This finding implies that while longer carbonization times may result in pore collapse and lower the material's adsorption effectiveness, longer impregnation times improve the activation process and the adsorption sites.

Using a 3D response plot, Figures 7 – (a), (b) and (c) show how the carbonization temperature (X_3) and carbonization time (X_4) affect the phenol index (Y_3). The phenol index rises with increasing carbonization temperatures and times, according to the surface plot, peaking at X_3 = 400°C and X_4 = 1.5 h. The phenol index starts to decline after this stage. According to this characteristic, adsorption efficiency is increased by moderate carbonization temperatures and durations, which also enhance pore structure development and active site availability.

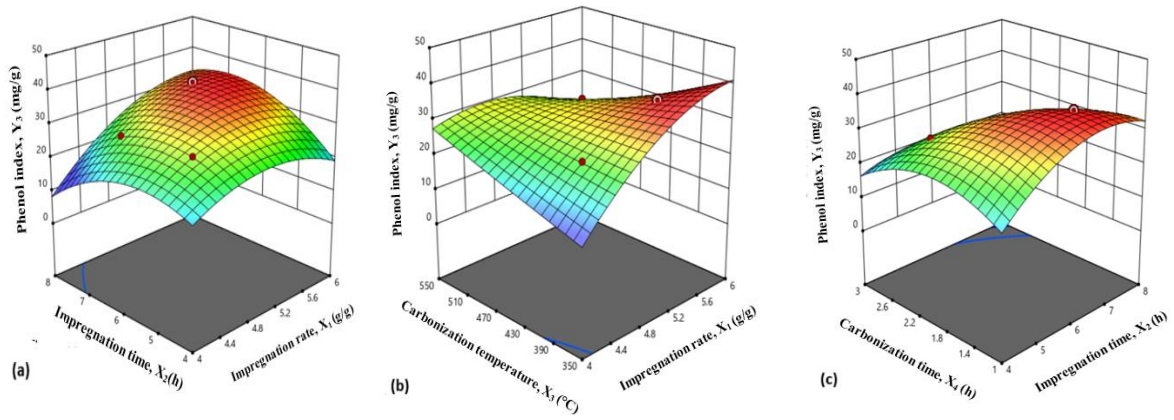

Fig. 7 3D response surface for response phenol index (Y3): **impregnation time and rate (X_1, X_2)** (a), impregnation rate (X_1) and carbonization temperature (X_3) (b), impregnation time (X_2) and carbonization time (X_4) (c).

Adsorption performance may be lowered by over carbonization or pore collapse brought on by extreme circumstances.

The analysis of Figures 5-6 and 7 reveals that the phenol index (Y_1) is significantly influenced by impregnation rate (X_1), impregnation time (X_2), carbonization temperature (X_3), and carbonization time (X_4). The optimal conditions for maximizing the phenol index involve an impregnation rate of approximately 5.5 g/g, an impregnation time of around 7 hours, a carbonization temperature near 400°C, and a carbonization time of approximately 1.5hours. These conditions favor the development of a well-structured porous network, enhancing the material's adsorption capacity. Conversely, deviations from these conditions, particularly excessive carbonization times, may degrade the pore structure, leading to reduced adsorption efficiency.

3.2.2. Multi-criteria optimization using desirability function

The objective of this study was to determine the optimal conditions for preparing activated carbon with desirable characteristics for wastewater treatment. The optimization of individual responses Y_1, Y_2, and Y_3 demonstrated that maximization of each response did not occur under the same experimental conditions. To identify a compromise solution, a multi-criteria optimization was conducted using the desirability function approach, implemented in the Design-Expert software, version 13.

3.2.3. Desirability function approach

The desirability function method is an effective approach for optimizing multiple outcomes in experiments by transforming each estimated response (Y_1, Y_2, and Y_3) into a desirability score. Each response is assigned a function that scales its values between 0 (undesirable) and 1 (ideal). Each estimated response (Y_i) is transformed into an individual desirability function (δi), which ranges from zero (undesirable, if $Y_i \leq Y_{i,\ min}$) to one (ideal, if $Y_i \geq Y_{i,\ max}$), where $Y_{i,min}$ and $Y_{i,max}$ represent the lower and upper acceptable limits for each response. These limits were determined based on quality criteria for the activated carbon used in wastewater treatment. Since the response surface was adequately explored within the range of studied variables, the weights for the responses (Y_1: iodine number, Y_2: MBI, and Y_3: phenol number) were all set to unity. Once the desirability function (δi) is defined for each response, the overall desirability function (Δ) is calculated as the geometric mean of the individual desirability, using the formula $\Delta = (\delta_1 \times \delta_2 \times \delta_3)^{1/3}$. This combined score ($\Delta$) indicates how well a specific set of conditions meets the overall objectives. Design-Expert software uses this combined score and maximizes it through its optimization tool, helping users determine the optimal settings for each variable.

The first three figures 8-(a), (b) and (c) illustrate the relationships between the experimental variables and the responses: iodine number (Y_1), methylene blue index (Y_2), and phenol index (Y_3). These 3D plots show how each response varies with changes in carbonization temperature, impregnation rate, and impregnation time. For example, Figure 9 highlights the variation in the iodine number as a function of impregnation rate and carbonization temperature. By visualizing these interactions, the desirability function approach effectively identifies the optimal conditions for each response.

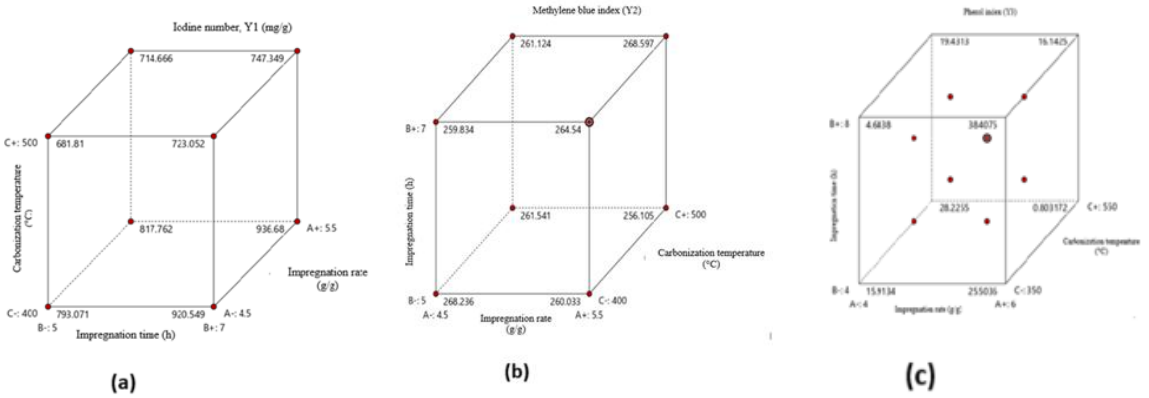

Fig. 8 Cube representation of experimental parameters affecting iodine number (a), methylene blue index (b), Phenol index (c)

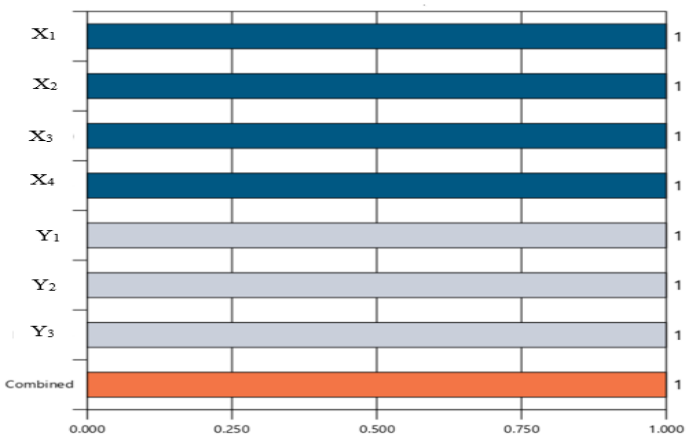

Fig. 9 Combined desirability score for optimization parameters

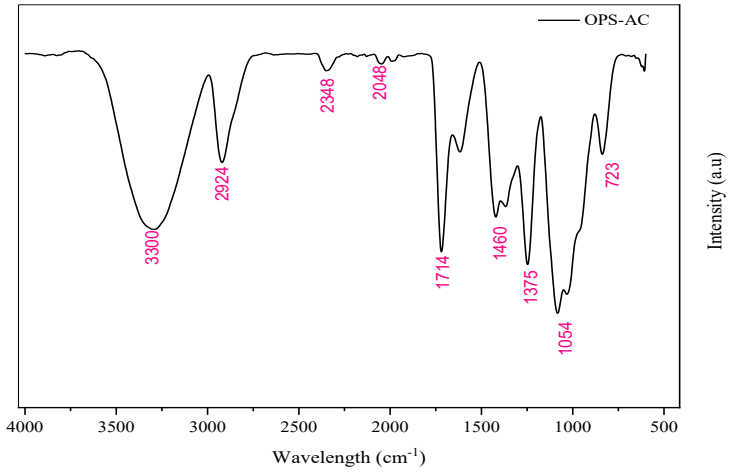

Fig. 10 FT-IR of activated carbon prepared under optimal conditions

Figure 9 presents the overall desirability assessment by combining individual desirability scores into a single metric, the combined desirability score (Δ). This score represents the extent to which the optimal conditions satisfy all response criteria simultaneously. The bar plot indicates that each response (Y_1, Y_2, Y_3) contributes equally, with a combined score of 1, demonstrating that the optimized conditions successfully maximize all desired outcomes. These visual representations validate the desirability function approach by illustrating individual and combined optimization performance. They provide a clear understanding of how the selected conditions meet the targeted quality criteria for the activated carbon.

3.3. Characterization of activated carbon prepared under optimal conditions

3.3.1. FTIR analysis

The FT-IR spectrum of activated carbon prepared under optimal conditions (impregnation ratio of 5.5 g/g, impregnation time of 7 h, carbonization temperature of 400°C, and carbonization time of 1.5 h, reveals several key features reflecting structural and chemical changes induced by the activation process (Figure 10). A broad band at 3300 cm^{-1} corresponds to O-H stretching vibrations associated with hydrogen-bonded hydroxyl groups. The reduced intensity of this band suggests a decrease in hydrogen bonding due to the dehydrating effect of activation. Peaks at 2924 cm^{-1}, attributed to asymmetric C-H stretching vibrations, show diminished intensity, indicating a reduction in aliphatic hydrogen content, which is supported by elemental analysis. The band at 1714 cm^{-1}, related to C=O stretching vibrations of carbonyl or carboxylic groups, also decreases significantly, implying the decomposition of oxygen-containing functional groups during thermal activation. In the region between 1640 and 1000 cm^{-1}, multiple peaks are observed, primarily associated with C=C aromatic stretching, C-O stretching, and C-H bending vibrations. These features indicate the development of aromatic structures and a reduction in oxygenated groups. Overall, the FT-IR spectrum demonstrates the transformation of olive pruning stems derived activated carbon, highlighting the loss of

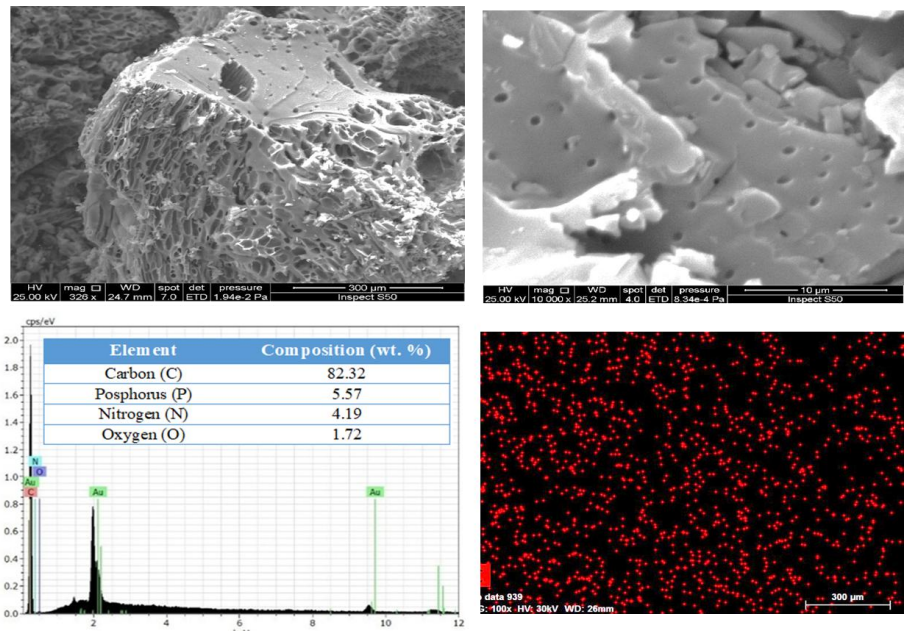

Fig. 11 SEM micrographs of activated carbon produced under the optimum's conditions

oxygen- and hydrogen-containing functional groups and the formation of aromatic carbon structures consistent with the expected effects of thermal decomposition and deoxygenation during activation.

3.3.2. Micrograph analysis

The SEM and EDX images presented in Figure 11 show the morphologies of activated carbon produced under the optimal conditions at different magnifications and measurement conditions. The structural and compositional modifications required for improved adsorption characteristics in activated carbon are confirmed by the SEM and EDX investigations (Jedynak and Charmas, 2024). The SEM images show notable alterations, including the formation of micropores and mesopores and a rough, uneven surface brought on by the breakdown of lignin, cellulose, and hemicellulose during carbonization and activation. Enhanced adsorption capacity is indicated by pore formation evidence. EDX images show successful activation and carbonization of activated carbon are indicated by a lower oxygen concentration and a higher carbon content.

3.3.3. The X-Ray Diffraction (XRD Analysis)

The XRD pattern of chemically activated OPS-AC reveals key structural features characteristic of amorphous carbon materials (Figure 12). A broad halo appearing at 20-30° (2θ) confirms the complete breakdown of the original biomass crystalline structure during carbonization, evidenced by the absence of characteristic cellulose peaks at 16° and 22°. Minor residual peaks suggest the presence of phosphorus-containing compounds, likely pyrophosphates (P_4O_{10}) derived from the H_3PO_4 activating agent. The diffraction profile demonstrates successful conversion to a disordered porous structure ideal for adsorption applications, while the lack of a graphite peak near 26° (2θ) indicates no significant graphitization occurred under these moderate activation conditions (Kim et al., 2023). These findings verify the effective production of amorphous activated carbon, though additional characterization is recommended to assess potential phosphorus residue effects on material performance.

3.3.4 N_2-adsorptiondesorption isotherm at 77 K

Figure 13 displayed the N2 adsorption-desorption isotherms at 77 K of OPS-AC produced by H_3PO_4 activation under optimum conditions, exhibits a high adsorption capacity for N_2 gas,

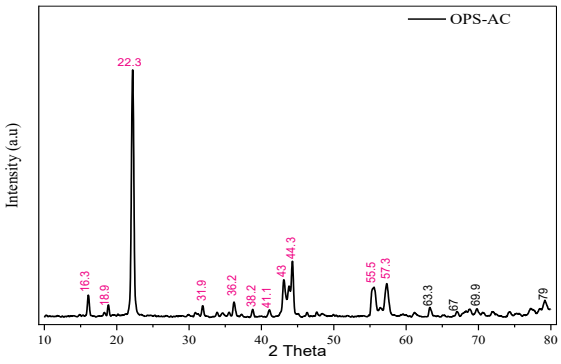

Fig. 12 X-ray diffraction (XRD) pattern of (OPS-AC)

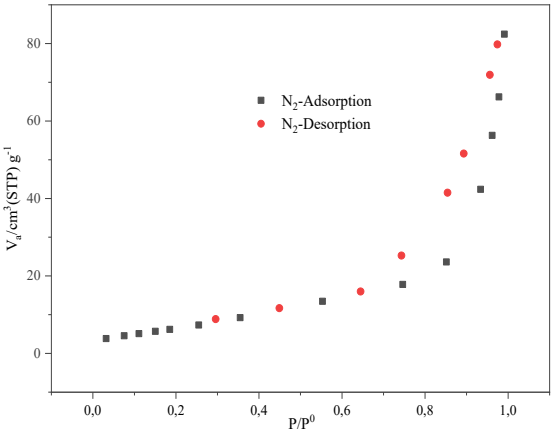

Fig. 13 N_2 adsorption–desorption isotherm on OPS-AC at 77

indicating a high surface area and important pore volume. As shown in table 5, The surface area of OPS-AC is 1604.8 m²/g with a correlation coefficient equal 0.9996, showing excellent agreement with the BET model., indicating a highly porous material with a total pore volume of 1.124 cm³/g and an average pore diameter of 20.815 nm.

The main of OPS-AC physical properties deduced from N_2 adsorption–desorption isotherm at 77 K is illustrated in table 5. Prepared activated carbon was characterized by a high important surface area of 1604.8 m²/g, with developed pore volume of 1.124 cm³/g and an average pore diameter of 20.81 nm.

3.4. Comparative performance analysis of OPS-AC to others synthesized ACs via chemical activation using H_3PO_4.

The activated carbon produced from olive pruning stems (OPS-AC) exhibits remarkable efficiency advantages compared to other activated carbons derived from agricultural by-products (Table 6). While materials such as olive kernels, date kernels, coconut shells, rice husks, and coffee grounds have been commonly used as precursors with phosphoric acid activation, OPS-AC demonstrated superior physicochemical properties. Despite a relatively high impregnation ratio (5.5:1 g/g) and a short activation period (7 hours), OPS-AC achieved a specific surface area (SBET) of 1604.8 m²/g, surpassing values reported for olive kernels (1460 m²/g; El-Hendawy, 2006), date kernels (1220 m²/g; Bouchelta, 2008), coconut shells (1350 m²/g; Daud et al., 2004), rice husks (1280 m²/g; Guo et al., 2017), and coffee grounds (1100 m²/g; Namane et al., 2005). This indicates a highly developed porous structure and enhanced surface functionality.

OPS-AC also displayed strong adsorption capabilities, with an iodine number of 947 mg/g, comparable to rice husks

Table 5
Physical properties of OPS-AC

Proprieties	Value	Unit
Multipoint BET	1604.85	$m^2\ g^{-1}$
Total Pore Volume (p/p_0=0.990)	1.124	$cm^3\ g^{-1}$
Average pore diameter	20.81	nm
R^2	0.9996	-

Table 6
Comparison of OPS-AC to others ACs

Raw Material	H_3PO_4 Ratio (g/g)	Impregnation Time (h)	Carbonization Temp. (°C)	Carbonization Time (h)	Iodine Index (mg/g)	Phenol Index (mg/g)	MB Index (mg/g)	SBET (m^2/g)	Reference
Coconut shell	2:1	24	450	1	1100	–	–	1350	(Daud et al., 2004)
Coffee grounds	1:1	24	450	1	–	210	–	1100	(Namane et al, 2005)
Olive stones	1.75	24	500	2	1020	–	–	1460	(El-Hendawy, 2005)
Date pits	1:1	24	500	2	950	–	380	1220	(Bouchelta, 2008)
Olive stones	1:1	24	500	2	–	–	–	950	(Al Ghouti, and Sweleh, 2019)
Pruning olive stems	5.5	7	400	1.5	947	35.63	267	1604.8	This work

(1050 mg/g) and olive kernels (1020 mg/g), reflecting efficient uptake of small molecules. The methylene blue adsorption capacity was 267 mg/g, slightly lower than rice husks (420 mg/g) and date kernels (380 mg/g), yet indicative of moderate mesoporosity for medium-sized molecules. Notably, the phenol adsorption capacity reached 35.63 mg/g, significantly higher than coffee residue (210 mg/g), demonstrating excellent potential for removing aromatic organic contaminants.

Moreover, the activation process was performed under relatively mild conditions—carbonization at 400 °C for 1.5 hours, lower than those typically used for other biomass precursors, highlighting both energy efficiency and economic feasibility. Collectively, these results establish OPS-AC as a sustainable and high-performance material for environmental applications, combining abundant raw material availability with superior adsorption properties and low preparation costs.

5. Conclusion

Valorizing olive pruning biomass as a precursor for chemically activated carbon using phosphoric acid offers an efficient and sustainable approach to transform this abundant agricultural by-product into a high-value material. Laboratory-scale optimization was performed to maximize the performance of the resulting activated carbon (AC), with Central Composite Design (CCD) applied to systematically refine preparation conditions. Olive wood proved to be an excellent precursor, producing AC with high efficiency for wastewater treatment applications. The experimental design allowed for the assessment of key factors, including the impregnation ratio, impregnation time, carbonization temperature, and carbonization duration—which were shown to significantly influence performance indicators such as the iodine number, methylene blue index, and phenol adsorption capacity. Multi-criteria optimization using desirability functions identified the optimal conditions as an impregnation ratio of 5.5:1 g/g, impregnation time of 7 hours, carbonization temperature of 400 °C, and carbonization time of 1.5 hours. Under these conditions, the resulting AC exhibited outstanding properties, including an iodine number of approximately 947 mg/g, a methylene blue index of 267 mg/g, a phenol adsorption capacity of 35.637 mg/g, and a high specific surface area of 1604.8 m^2/g. The material displayed pronounced mesoporosity, indicating strong potential not only for adsorption in water treatment but also for broader applications in catalysis and energy storage. Overall, olive pruning wood represents an effective and sustainable feedstock for high-performance activated carbon, highlighting its value for environmental and industrial applications.

Acknowledgements

The authors wish to convey their sincere appreciation and gratitude to the Research Laboratory: Process Engineering and Industrial Systems, (LR11ES54) at the National School of Engineers of Gabes, (ENIG), University of Gabes, where this work was conducted.

Author Contributions: Ismaeel Ahmed Nagim: Writing – original draft, Visualization, Conceptualization. Methodology. Thouraya Bohli: Writing – original draft, review and editing, Supervision, Methodology. Abdelmottaleb Ouederni Validation, Supervision, review.

Funding: The author(s) received no financial support for publication of this article.

Conflicts of Interest: The authors declare that they have no known competing financial interests or personal relationships that could have appeared to influence the work reported in this paper.

References

Abdelnaeim, M. Y., El Sherif, I. Y., Attia, A. A., Fathy, N. A., El-Shahat, M. F. (2016). Impact of chemical activation on the adsorption performance of common reed towards Cu(II) and Cd(II). *International Journal of Mineral Processing*, 157, 80–88. https://doi.org/10.1016/j.minpro.2016.09.013

Ahmed, M. J., and Hameed, B. H. (2020). Advances in biomass waste valorization. *Journal of Cleaner Production*, 287, 125011. https://doi.org/10.1016/j.jclepro.2020.125011

Ahmed, M. J., Theydan, S. K. (2012). Physical and chemical characteristics of activated carbon prepared by pyrolysis of chemically treated date stones and its ability to adsorb organics. *Powder Technology*, 229, 237–245. https://doi.org/10.1016/j.powtec.2012.06.043

Al-Qahtani, K. M., Al-Zahrani, M. A. (2021). Pharmaceutical adsorption. *Journal of Molecular Liquids*, 334, 116074. https://doi.org/10.1016/j.molliq.2021.116074

Al Ghouti, M. A., Sweleh, A. O. (2019). Optimizing textile dye removal by activated carbon prepared from olive stones. *Environmental Technology & Innovation,* 16, 100488. https://doi.org/10.1016/j.eti.2019.100488

Alslaibi, T. M., Abustan, I., Ahmad, M. A., Abu Foul, A. A. (2013). A review: Production of activated carbon from agricultural by-products via conventional and microwave heating. *Journal of Chemical Technology & Biotechnology,* 88(7), 1183–1190. https://doi.org/10.1002/jctb.4028

Arokiadass, R., Palaniradja, K., Alagumoorthi, N. (2012). Prediction and optimization of end milling process parameters of cast aluminium

based MMC. *Transactions of Nonferrous Metals Society of China,* 22(7), 1568-1574. https://doi.org/10.1016/S1003-6326(11)61356-9

Araujo, C. S., Alves, V. N., Rezende, H. C. (2018). Activated carbon from coconut fibers for dye removal. *Journal of Environmental Chemical Engineering*, 6(2), 1714–1721.

ASTM D4607-94, Standard test method for determination of iodine number of activated carbon, ASTM International, 2006.

AWWA B600-90, Standard for sodium hydroxide (caustic soda), American Water Works Association, 1990.

Balogoun, C., Bawa, M., Osseni, S., Aina, M. (2015). Preparation of activated carbons by chemical means with phosphoric acid based on coconut shell. *International Journal of Biological and Chemical Sciences,* 9(1), 563. https://doi.org/10.4314/ijbcs.v9i1.48

Bayuo, J., Abukari, M. A., Pelig-Ba, K. B. (2020). Optimization using central composite design (CCD) of response surface methodology (RSM) for biosorption of hexavalent chromium from aqueous media. *Applied Water Science*, 10, 135. https://doi.org/10.1007/s13201-020-01213-3

Bedia, J., Peñas-Garzón, M., Gómez-Avilés, A., Rodríguez, J. J., Belver, C. (2020). Review on activated carbons by chemical activation with $FeCl_3$. *C - Journal of Carbon Research*, *6*(2), 21. https://doi.org/10.3390/c6020021

Bhattacharya, S. S., Bhattacharya, A., Singh, N. (2019). Functionalization of activated carbon: A review of synthesis methods, properties, and applications. *Environmental Chemistry Letters, 17*(1), 287-303. https://doi.org/10.1007/s10311-018-00820-w

Bohli, T., Bourezgui, A., Maiz, F., Ouederni, A., (2025). Removal of a pharmaceutical compound using olive stone-derived activated carbon: Artificial neural network modeling, equilibrium analysis, and fixed-bed kinetic assessment. MaterialsToday Communications, 45, p. 112200. https://doi.org/10.1016/j.mtcomm.2025.112200

Bohli, T., Ouederni A., Villaescusa, I., (2017). Simultaneous adsorption behavior of heavy metals onto microporous olive stones activated carbon: analysis of metal interactions. *Euro-Mediterr J Environ Integr,* 2,19. https://doi.org/10.1007/s41207-017-0030-0

Bohli, T., Ouederni, A., Fiol, N., Villaescusa, I., (2015). Evaluation of an activated carbon from olive stones used as an adsorbent for heavy metal removal from aqueous phases, *Comptes Rendus Chimie* 18(1), 88-99. https://doi.org/10.1016/j.crci.2014.05.009

Bouchelta, C., Salah Medjram M., Bertrand O., Bellat P.J. (2008). Preparation and characterization of activated carbon from date stones by physical activation. *Journal of Analytical and Applied Pyrolysis,* 82 (1), 70–77. https://doi.org/10.1016/j.jaap.2007.12.009

Box, G. E. P., Wilson, K. B. (1951). On the experimental attainment of optimum conditions. *Journal of the Royal Statistical Society. Series B (Methodological),* 13(1), 1–45. https://doi.org/10.1111/j.2517-6161.1951.tb00067.x

Chelladurai, S. J. S., Murugan, K., Ray, A. P., Upadhyaya, M., Narasimharaj, V., Gnanasekaran, S. (2021). Optimization of process parameters using response surface methodology: A review. *Materials Today: Proceedings.* https://doi.org/10.1016/j.matpr.2020.06.466

Chen, X., Pei, Y., Wang, X., Zhou, W., Jiang, L. (2024). Response surface methodology—Central composite design optimization sugarcane bagasse activated carbon under varying microwave-assisted pyrolysis conditions. *Processes,* 12(3), 497. https://doi.org/10.3390/pr12030497

Chen, X., Chen, G., Chen, L., Chen, Y., Lehmann, J., McBride, M. B., Hay, A. G. (2022). Banana peel biochar for enhanced removal of ammonium and phosphate from aqueous solutions. *Journal of Environmental Management,* 302, 114073. https://doi.org/10.1016/j.jenvman.2021.114073

Daud, W. M. A. W., Ali, W. S. W. (2004). Comparison on pore development of activated carbon produced from palm shell and coconut shell. *Bioresource Technology,* 93 (1), 63–69. https://doi.org/10.1016/j.biortech.2003.09.015

Debbache, H., et al. (2024). Chemical activation to produce activated carbon: influence of activating-agent type, impregnation ratio, pyrolysis temperature and residence time on textural and adsorption properties. *Cellulose Chemistry and Technology*, 58(9-10), 1149-1161.

Devi, R., Kumar,V., Kumar, S., Bulla, M. (2023). Recent advancement in biomass-derived activated carbon for waste water treatment, energy storage, and gas purification : a review, Journal of Materials Science 58(30):1-24. https://doi.org/10.1007/s10853-023-08773-0

El-Hendawy, A. N. A. (2006). Surface and adsorptive properties of carbons prepared from biomass. Journal of Analytical and Applied Pyrolysis, 75 (2), 159–166. https://doi.org/10.1016/j.jaap.2005.05.004

El-Sayed, S.A., Khass, T.M. and Mostafa, M.E. (2024) 'Thermal degradation behaviour and chemical kinetic characteristics of biomass pyrolysis using TG/DTG/DTA techniques', *Biomass Conversion and Biorefinery,* 14, 17779-17803. https://doi.org/10.1007/s13399-023-03926-2

González-Serrano, E., Gómez-Serrano, V., Valenzuela-Calahorro, C., González-García, C. M. (2021). Surface chemistry studies on activated carbon by wet oxidation: Effect of oxygen surface groups on aqueous-phase adsorption. *Carbon,* 179, 1–10. https://doi.org/10.1016/j.carbon.2021.03.048

González-García, P. (2018). Lignocellulosics precursors review. Renewable and Sustainable Energy Reviews, 82, 1393-1414. https://doi.org/10.1016/j.rser.2017.04.117

Gupta, V. K., Verma, N. (2019). Sustainable production of activated carbon from biomass. *Journal of Environmental Management, 240*, 25–34. https://doi.org/10.1016/j.jenvman.2019.03.062

Hassan, M. M., Carr, C. M., Islam, M. S. (2015). A critical review on recent advancements of the removal of reactive dyes. *Chemosphere*, 209, 201-219. https://doi.org/10.1016/j.chemosphere.2018.06.043

Hendronursitoa, Y., Astutib, W., Sabarmana, H., Santoso I. (2025) A porous activated carbon derived from banana peel by hydrothermal activation two-step methods. *Int. J. Renew. Energy Dev.*(14)2, 322-331. https://doi.org/10.61435/ijred.2025.60847

Jaria, G., Silva, C.P., Oliveira, J.A.B.P., Santos, S.M., Gil, M., V., Otero,M., Calisto,V., Esteves V.I. (2019). Production of highly efficient activated carbons from industrial wastes for the removal of pharmaceuticals from water—A full factorial design, *J. of Hazardous Materials,* 370 (15), 212-218. https://doi.org/10.1016/j.jhazmat.2018.02.053

Jedynak, K., & Charmas, B. (2024). Application of activated carbons obtained from polymer waste for the adsorption of dyes from aqueous solutions. *Materials,* 17(3), 748. https://doi.org/10.3390/ma17030748

Jeguirim, M., Limousy, L, and S. Bennici, S. (2020). Biomass-derived chars for energy applications, *Renew. Sustain. Energy Rev.*, 108, pp. 253–273. https://doi.org/10.1016/j.rser.2019.03.057.

Kamińska, A., Miądlicki,P., Kiełbasa, K., Kujbida, M., Sreńscek-Nazzal, J., Wróbel, R.J., Wróblewska,A. (2021). Activated Carbons Obtained from Orange Peels, Coffee Grounds, and Sunflower Husks—Comparison of Physicochemical Properties and Activity in the Alpha-Pinene Isomerization Process. *Materials* 14(23), 7448; https://doi.org/10.3390/ma14237448

Kang, DJ, Kim, KW, Hong, BU, Park, JE. (2024). Production of high specific surface area activated carbon from tangerine peels and utilization of its by-products. *Energies, 17*(23), 6148. https://doi.org/10.3390/en17236148

Kim, J.-H., Kim, Y.-J., Kang, S.-C., Lee, H.-M., Kim, B.-J. (2023). Preparation and characterization of asphalt pitch-derived activated carbons with enhanced electrochemical performance as EDLC electrode materials. *Minerals,* 13(6), Article 802. https://doi.org/10.3390/min13060802

Khalid, A. A., Gora, A. M., Rafindadi, A. D., Haruna, S. I., Ibrahim, Y. E. (2024). Response Surface Methodology Approach for the Prediction and Optimization of the Mechanical Properties of Sustainable Laterized Concrete Incorporating Eco-Friendly Calcium Carbide Waste. *Infrastructures,* 9(11), 206. https://doi.org/10.3390/infrastructures9110206

Li, B., Hu, J., Xiong, H., Xiao, Y. (2020). Application and properties of microporous carbons activated by $ZnCl_2$: Adsorption behavior and activation mechanism. *ACS Omega*, 5(18), 9398–9407. https://doi.org/10.1021/acsomega.0c00461

Liu, G., Zhang, C., Dou, D., Wei, Y. (2021). Modeling and optimization of activated carbon carbonization process based on support vector machine.*Physicochemical Problems of M*ineral Processing. https://doi.org/10.37190/PPMP/133057

Liu, S., Chen, Z., Shen, Y., Chen, H., Li, Z., Cai, L., Yang, H., Zhu, C., Shen, J., Kang, J., Yan, P., (2024). Simultaneous regeneration of activated carbon and removal of adsorbed atrazine by ozonation process: From laboratory scale to pilot studies. *Water Research,* 251, 1,121113. https://doi.org/10.1016/j.watres.2024.121113

Liu, W.J., Jiang, H., & Yu, H.-Q. (2015). Development of biochar-based functional materials: Toward a sustainable platform carbon material. *Chemical Reviews*, 115(22), 12251–12285. https://doi.org/10.1021/acs.chemrev.5b00195

Lütke, S. F., Igansi, A. V, Pegoraro, L., Dotto, G. L., Pinto, L. A. A., Cadaval, T. R. S. (2019). Journal of Environmental Chemical Engineering Preparation of activated carbon from black wattle bark waste and its application for phenol adsorption. *Journal of Environmental Chemical Engineering,* 7(5), 103396. https://doi.org/10.1016/j.jece.2019.103396

Lix, L. M., Keselman, J. C., & Keselman, H. J. (1996). Consequences of assumption violations revisited: A quantitative review of alternatives to the one-way ANOVA F-test. *Review of Educational Research,* 66(4), 579-619. https://doi.org/10.3102/00346543066004579

Louarrat, M., Enaime, G., Baçaoui, A., Yaacoubi, A., Blin, J., Martin, L. (2019). Optimization of conditions for the preparation of activated carbon from olive stones for application in gold recovery. *Journal of the Southern African Institute of Mining and Metallurgy*, 119(3), 281–288. https://doi.org/10.17159/2411-9717/2019/v119n3a9

Maceiras, R., Álvarez, E., & Cancela, M. Á. (2017). Applications of activated carbon in environmental protection. *Environmental Science and Pollution Research*, 24(6), 5237-5247. https://doi.org/10.1007/s11356-016-8224-6

Molina-Sabio, M., & Rodríguez-Reinoso, F. (2004). Role of chemical activation in the development of carbon porosity. *Colloids and Surfaces A: Physicochemical and Engineering Aspects,* 241(1–3), 15–25. https://doi.org/10.1016/j.colsurfa.2004.04.007

Namane, A., Mekarzia, A., Benrachedi, K., Belhaneche-Bensemra, N., Hellal, A. (2005). Determination of the adsorption capacity of activated carbon made from coffee grounds by chemical activation with $ZnCl_2$ and H_3PO_4. *Journal of Hazardous Materials,* 119(1–3), 189–194. https://doi.org/10.1016/j.jhazmat.2004.12.006.

Paz, E. C. S., Paschoalato, C. F., Arruda, M. G., Silva, G. G., Santos, M. L. G., Pedroza, M. M., Oliveira, L. R. A. (2023). Production and characterization of the solid product of coconut pyrolysis. Biomass Conversion and Biorefinery, 13, 6317–6329. https://doi.org/10.1007/s13399-021-01561-3

Ponce, M. F., Mamani, A., Jerez, F., Castilla, J., Ramos, P. B., Acosta, G. G., Sardella, M. F., Bavio, M. A. (2022). Activated carbon from olive tree pruning residue for symmetric solid-state supercapacitor. Energy, 260, 125092. https://doi.org/10.1016/j.energy.2022.125092

Rahman, M.S., Bansal, N., Rahman, M.H., Mortula, M. (2025). Date Seed-Derived Activated Carbon: A Comparative Study on Heavy Metal Removal from Aqueous Solutions, Appl. Sci., 15(6), 3257. https://doi.org/10.3390/app15063257

Raposo, F., De la Rubia, M. A. Borja, R. (2008). Methylene Blue Number as Useful Indicator to Evaluate the Adsorptive Capacity of Granular Activated Carbon in Batch Mode: Influence of Adsorbate/Adsorbent Mass Ratio and Particle Size. Journal of Hazardous Materials 165(1-3):291-9. https://doi.org/10.1016/j.jhazmat.2008.09.106

Saadi, W., Najar Souissi, S., Ouederni, A., (2016) Pomegranate Peels Precursor Used in the Synthesis of Activated Carbon: Application in the Wastewater Treatment, *J. Int. Environmental Application & Science*, 11(4), 318-330. https://dergipark.org.tr/tr/download/article-file/570653

Sun, Z., Wang, M., Fan, J., Zhou, Y., Zhang, L. (2024), Regeneration Performance of Activated Carbon for Desulfurization. Appleid Sciences 10(17):6107. https://doi.org/10.3390/app10176107

Tan, X., Liu, Y., & Zeng, G. (2016). Application of biochar for pollutant removal. *Environmental Science and Pollution Research*, 23(17), 16904–16917. https://doi.org/10.1007/s11356-016-6964-y

Trache, D., Khimeche, K., Mezroua, A., Benziane, M., (2016). Physicochemical properties of microcrystalline nitrocellulose from Alfa grass fibres and its thermal stability. *Journal of Thermal Analysis and Calorimetry*, 124(3):1485–1496. https://doi.org/10.1007/s10973-016-5293-1.

Wang, Y., Jiang, H., Guo, Z., Ma, H., Wang, S., Wang, H., Song, S., Zhang, J., Yin, Y., Wu, H., Jiang, Z., & Guiver, M. D. (2023). Advances in organic microporous membranes for CO_2 separation. *Energy & Environmental Science*, 16(1), 53–75. https://doi.org/10.1039/D2EE02449G

Yaashikaa, P. R., Kumar, P. S., Varjani, S. J., & Saravanan, A. (2020). A review on photochemical, biochemical and electrochemical transformation of CO_2 into value-added products. *Journal of CO2 Utilization,* 33, 131–147. https://doi.org/10.1016/j.jcou.2019.05.017

Yakout, S. M., & El-Deen, G. S. (2012). Characterization of activated carbon from olive stones. *Arabian Journal of Chemistry*, 5(2), 219-229. https://doi.org/10.1016/j.arabjc.2010.09.003

Zaid, H., Al-Sharify, Z., Hamzah, M. H., & Rushdi, S. (2024). Optimization of different chemical processes using response surface methodology – a review. *Journal of Engineering and Sustainable Development,* 26(6). https://doi.org/10.31272/jeasd.26.6.1

Zakaria, R., Jamalluddin, N. A., & Abu Bakar, M. Z. (2021). Effect of impregnation ratio and activation temperature on the yield and adsorption performance of mangrove-based activated carbon for methylene blue removal. *Results in Materials*, 10, 100183. https://doi.org/10.1016/j.rinma.2021.100183

Zhao, S., Yan, T., & Wang, Z. (2017). Facile control of corncobs-based carbons with eutectic salt $ZnCl_2$/NaCl templated for the adsorption of organic aldehyde. *BioResources*, 14(4), 8835–8848. https://doi.org/10.15376/biores.14.4.8835-8848

Zhou, Y., Zhang, J., Wang, L., Cui, X., Liu, X., Wong, S. S., & Luo, Y. (2021).
Self-assembled iron-containing mordenite monolith for carbon dioxide sieving. *Science,* 373(6557), 315–320. https://doi.org/10.1126/science.aax5776